



Oxide Formation and Dissolution on Silicon in KOH Electrolyte: An In-Situ Infrared Study

H. G. G. Philipsen,^{a,b,c} F. Ozanam,^{b,*} P. Allongue,^{b,*} J. J. Kelly,^a and J.-N. Chazalviel^{b,d,*z}

^aDebye Institute for Nanomaterials Science, Utrecht University, 3508 TA Utrecht, The Netherlands

^bPhysique de la Matière Condensée, CNRS-Ecole Polytechnique, 91128 Palaiseau, France

The n-Si(111)/6 M KOH electrolyte interface has been investigated by in-situ multiple-internal reflection infrared spectroscopy, at room temperature and at 40°C. The potential was stepped successively to positive and negative values with respect to open-circuit potential, during which surface oxidation and oxide dissolution occur, respectively. Infrared spectra were recorded together with the interfacial current. Analysis of the spectra indicates that formation of an oxide layer at the positive potential takes place in two steps: a first step associated with replacement of the surface SiH by SiOH or SiO⁻ groups, and a second step, associated with the formation of SiOSi groups and growth of a passivating oxide layer. The mechanism is strongly dependent on the competition between oxidation and dissolution, which accounts for the complex shape of the current transient and its temperature dependence. At the negative potential, dissolution of the oxide takes place by random pitting, until the hydrogenated surface is restored.

© The Author(s) 2016. Published by ECS. This is an open access article distributed under the terms of the Creative Commons Attribution 4.0 License (CC BY, <http://creativecommons.org/licenses/by/4.0/>), which permits unrestricted reuse of the work in any medium, provided the original work is properly cited. [DOI: 10.1149/2.0911605jes] All rights reserved.

Manuscript submitted December 21, 2015; revised manuscript received January 29, 2016. Published February 11, 2016.

The surface chemistry of silicon in KOH and other alkaline electrolytes has been the subject of numerous investigations stimulated by interest in its anisotropic chemical etching properties, surprising features in the electrochemistry and important applications related to such properties.^{1–4} For a brief overview of this field we refer the reader to the introduction of a previously published paper.⁵ In that work we used a combined real time electrochemical/in-situ infrared (IR) spectroscopy approach to investigate the surface chemistry of Si in KOH solution on stepping the potential of an n-type Si(111) electrode between a value negative of open-circuit potential (OCP) in the range of cathodic hydrogen evolution and a value in the passive range at which an oxide film is formed. The spectral baseline and the Si-H stretching (ν_{SiH}) spectral range were analyzed in detail. The change in the spectral baseline indicated that the electronic state of the surface switches from electron accumulation at the negative potential to inversion at the positive potential. At the same time hydrogen termination of the surface^{6,7} disappears. When the potential is switched back to its negative value, the initial hydrogenated surface is recovered after an induction time. Furthermore, incorporation of cathodically generated hydrogen into Si was found to occur in the form of dilute centers, then accumulation of the associated stress leads to the formation of microcracks partially decorated with hydrogen.⁵

In the present paper we concentrate on the mechanisms of anodic oxidation of n-Si(111) and dissolution of the anodic oxide. An especially intriguing aspect of the electrochemistry of n-Si in KOH solution is the strong orientation dependence of oxide formation when the potential of the electrode is switched from a value negative of OCP to one in the passive range, as shown by the current transients in Fig. 1 (after Ref. 8).⁸ The remarkable point in Fig. 1 is the fact that the (100) surface is immediately oxidized (see fast decay of the anodic current, curve (100), Fig. 1) whereas oxidation of the (111) surface is much slower. Smith et al. suggested that the corresponding current transients (see curve (111) in Fig. 1) consist of two overlapping peaks that they attributed to the transformation of the native “chemical” oxide into an “electrochemical” oxide, followed by island growth of a passivating oxide layer.⁹ However, as recalled in the introduction of Ref. 5, it is now well established that the silicon surface in alkaline solution is hydrogen terminated at OCP.^{6,7} A second surprising aspect of the results of Fig. 1 is the observation of a significant anodic current density with n-type electrodes in the dark, though oxide formation on semiconductors generally requires valence band holes.

Clearly, the mechanisms of anodic oxidation and oxide dissolution need to be reconsidered. This requires chemical information about the surface reactions. In the present paper we focus again on n-Si(111) in 6 M KOH solution, considering oxide formation at the positive potential and oxide dissolution at the negative potential, using real-time electrochemical in-situ IR spectroscopy. We perform a detailed analysis of the oxide- and OH-related bands and explore how these results can be accounted for within the framework of a theoretical mechanism. Finally, we discuss briefly the issue of charge transfer and the strong anisotropy observed in anodic oxidation.

Experimental

The details of the experimental procedure have been given in the previous paper.⁵ Briefly, the IR spectra were taken in the multiple-internal-reflection geometry,¹⁰ at room temperature (RT) and at 40°C. The electrolyte was 6 M KOH, and the n-Si electrode was (111)-oriented, P-doped (130–150 Ωcm resistivity, 500 μm thickness). The potential was stepped between –1.3 V and +1.0 V vs mercury/mercurous sulfate reference. The spectra were converted to differential absorbance spectra by choosing a reference state (e.g., the steady state at the negative potential) and calculating $(1/N)\ln[I_0(\sigma)/I(\sigma)]$, where σ is wave number, $N = 10$ is the number of useful reflections at the Si/electrolyte interface, $I_0(\sigma)$ is the raw spectrum (i.e., spectrum of the light reaching the detector) in the reference state and $I(\sigma)$ is the raw spectrum in the state under consideration. Analysis of these differential spectra was performed by using a

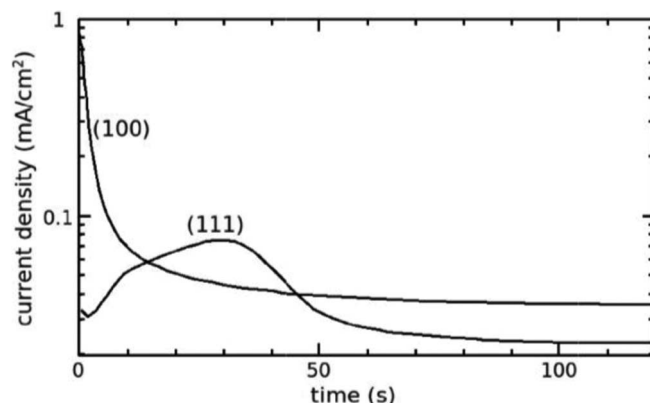


Figure 1. Typical current transients obtained upon stepping the potential from OCP to 0 V vs SCE reference. n-Si electrode in 5 M KOH at 55°C, for (100) and (111) orientations (after Ref. 8).

*Electrochemical Society Active Member.

^aPresent address: IMEC, Leuven, Belgium.

^bPresent address: 25 rue Eugène Combes, 19800 Corrèze, France.

^cE-mail: jean-noel.chazalviel@polytechnique.edu

Table I. Summary of the various vibrational contributions considered in analyzing the spectra.

Notation	Position (cm^{-1})	Assignment
NBO	940	νSiO in SiOH or SiO^-
TO	ca 1050	νSiO in SiOSi (vibration parallel to the surface)
D	ca 1150	νSiO in SiOSi (isolated siloxane / disorder mode)
LO	ca 1200	νSiO in SiOSi (vibration perpendicular to the surface)
electrolyte	3300–3400	νOH in H_2O
electrolyte	1640	δOH_2 in H_2O
SiOH(f)	ca 3600	νOH in “free” (or weakly H-bonded) SiOH
SiOH(hb)	3000–3300	νOH in hydrogen-bonded non-bridging oxygen (NBO) sites ($\text{SiOH}\cdots\text{OH}_2$, $\text{SiOH}\cdots\text{OH}$, or $\text{SiO}\cdots\text{HOH}$)
miscellaneous	2855–2930	νCH (O-ring seal)
miscellaneous	1400–1550	O-ring seal

versatile home-made fitting software. In the following, the fitting methods for each spectral range will be mentioned only briefly, the technical details being given in the Appendix, together with an assessment of the reliability of the results (see also Supplementary Material I: Residuals, confidence intervals and correlation matrices for some typical fits). At a general level, and besides the details given in the Appendix, note that fitting several hundreds of spectra with a common method is a very demanding task, and the consistent fitting of the whole series stands as a stringent test of the model used for fitting.

Results

The results of the experiments at RT and at 40°C showed marked differences, which were found to be reproducible over many experiments. Also, as reported in detail in Ref. 5, the baseline in the data at 40°C is dominated by a broad band centered around 3000 cm^{-1} (electronic transition associated with hydrogen penetration into the silicon lattice, a contribution that does not appear in the RT data), which makes the extraction of the vibrational signals more difficult.⁵ For these reasons, we will present the results at RT and at 40°C in two separate subsections. The IR bands considered are listed in Table I.

The RT study.—The essential features of a room-temperature experiment (potential cycle, current transients, collection of spectra) are summarized in Fig. 2. As discussed in our previous paper,⁵ the strong variation of the baseline is mostly due to a change in free-carrier absorption (Drude absorption + interband transition) associated with a change in band bending induced by the potential change. For the n-Si(111) electrode, electron accumulation conditions prevail at potentials negative of OCP (here –1.25 V) and the surface is H-terminated. Upon stepping the potential to a value positive of OCP (here +1 V), about 2/3 of the H-monolayer instantaneously disappears and on a longer time scale (ca 200 s), an inversion layer sets in and the remaining SiH groups disappear, indicating progressive oxidation. Note that the anodic current transient in Fig. 2b is much weaker and extends to much longer times than that in Fig. 1, a difference mainly due to the lower temperature of the experiment of Fig. 2.⁵ In the present paper we will focus on the bands characteristic of oxide formation.

Si-O stretching (νSiO) region.—Typical spectra of the νSiO region after baseline subtraction are shown in Fig. 3. The conspicuous effect of polarization, indicative of the formation of a compact silicon dioxide film, has led us to perform a detailed analysis of these spectra.

Previous studies.—The νSiO absorption of anodic films of silica is well known from previous work.¹¹ In s polarization, three bands are present: i) the non-bridging oxygen band (NBO), centered at 940

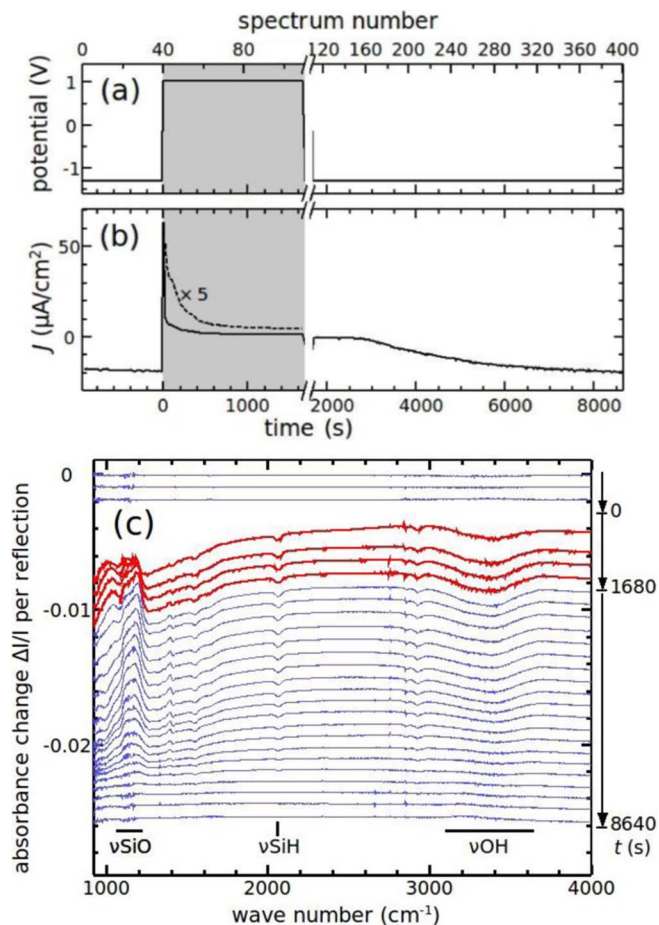


Figure 2. Typical room-temperature results for n-Si in 6 M KOH. (a) Potential cycle. The upper scale gives the correspondence between time and spectrum number within a cycle (400 spectra per cycle). (b) Resulting current transients. The gray shading in (a) and (b) indicates the time spent at the positive potential. Note the scale break at the time of the negative-potential step ($t = 1680$ s, spectrum #110). (c) Series of IR spectra, recorded in p polarization. The reference was taken in the steady state at the negative potential. The spectra shown here are the result of a double averaging: average of packets of 5 consecutive spectra, and average of 3 consecutive cycles (hence, 400:5 = 80 spectra; only 1 out of 3 shown). For clarity, the curves have been shifted vertically by increments of –0.001. The spectra recorded at the positive potential are drawn as bold red lines, those recorded at the negative potential as thin blue lines. The time scale is shown on the right-hand side. Note the sudden change in baseline (loss of the strong-electron-accumulation layer) following the positive potential step ($t = 0$).

cm^{-1} , ii) the main band (so-called transverse optical, TO) at around 1050 cm^{-1} , iii) a “disorder” (D) band at around 1100–1150 cm^{-1} . In p polarization, two extra bands appear, which consist of the longitudinal counterparts of the D and TO bands (the appearance of these bands in p polarization is also known as the Berreman effect¹²). The former band lies at a somewhat lower energy than the transverse D band but is largely overlapping it,¹³ which may justify describing them as a single band whose position and width change between s- and p-polarization. The latter band (so-called longitudinal optical, LO) is located at 1254 cm^{-1} for dry thermal silica but may be shifted down to around 1200 cm^{-1} for anodic silica.^{11,13–15}

Fitting procedure.—Analysis of the spectra requires attention to the sloping baseline arising from the loss of the free-carrier accumulation layer when the potential is stepped to a positive value.⁵ The fitting procedure is described in detail in the Appendix, Sec. II. In brief, the three bands in s polarization were taken as Gaussian curves, and the characteristics of the NBO band (center at 940 cm^{-1} , FWHM 120 cm^{-1}) were kept fixed, because they are known from previous work,¹¹ and cannot justifiably be taken as adjustable parameters, due

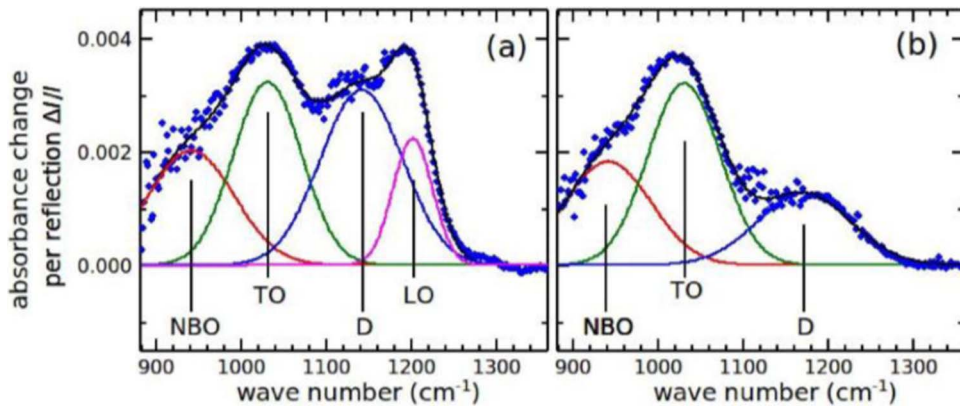


Figure 3. Typical RT spectra in p polarization (a) and s polarization (b) in the vSiO region. Here data at $t = 1680$ s (last spectrum at the positive potential). The experimental data (blue dots) are shown after baseline subtraction. The spectral decomposition includes four vibrational bands (NBO, TO, D, LO for p polarization only), shown as thin lines. See text and Appendix, Sec. II for details.

to the high noise level in this region. In p polarization, the LO band was added, but a single D band was kept as it was found difficult to resolve the two disorder bands in the p-spectra. As mentioned above, this implies that the center of the disorder band may be somewhat shifted to lower energy in p polarization, and its intensity may be significantly larger in p polarization than in s polarization.¹³ The fits of the spectra in Fig. 3 are also shown, together with the different Gaussian contributions. The fits are good and the confidence limits of the parameters are at most of a few percent. However, note that the fits of the lower-energy bands, and especially that of the NBO band, are baseline-sensitive (for more details, see Supplementary Material I). Hence, the results for the intensity of this band must be taken with some caution, but this uncertainty has a minor impact on the total intensity of the vSiO band.

General trends.—Figure 4 shows the time dependence of the different band intensities in p polarization (Fig. 4a) and s polarization

(Fig. 4b), as obtained from the fits. The time dependence of the intensity is seen to be markedly different for the various bands. These features are especially apparent in the p-spectra. On the positive-potential step, the NBO- and D-bands appear immediately at the first spectrum after the potential step ($t = 0$) and subsequently undergo a weak variation (the NBO band exhibiting a slow decline in the p-spectra). The TO- and LO-bands appear more progressively, say on the scale of ~ 200 s. On the negative-potential step, the D band is initially stable and in the p-spectra even exhibits a slow increase. On the other hand, the NBO band decreases, while the TO and LO bands show an even faster decrease.^e At an intermediate stage (around $t = 4000$ s), the NBO- and TO-bands remain approximately constant and in the p-spectra even seem to exhibit a small re-increase followed by a broad maximum (it is not clear whether this re-increase is meaningful). In a last stage, all of the four bands decay to zero.^f

Salient features.—These results indicate that the variation of the intensity of the “dry-oxide” (TO and LO) bands is non-trivial: during oxide formation, the growth of these bands is somewhat delayed with respect to that of the NBO and D bands. During oxide dissolution, they exhibit a marked initial decrease contrasting with the weaker variation of the NBO and D bands, before all four bands decay to zero. The origin of these trends will be addressed in the Discussion section.

O-H stretching (vOH) region.—Figure 5 shows two typical spectra in the vOH region; the first one (Fig. 5a) was recorded just after the positive-potential step, and the second (Fig. 5b) just before the negative-potential step. Interestingly, the shape of the two spectra shown is quite different: the spectrum in Fig. 5b appears dominated by a negative contribution proportional to electrolyte absorption, as might be expected from the formation of a solid film between the silicon and the electrolyte;¹⁰ whereas the spectrum in Fig. 5a essentially consists

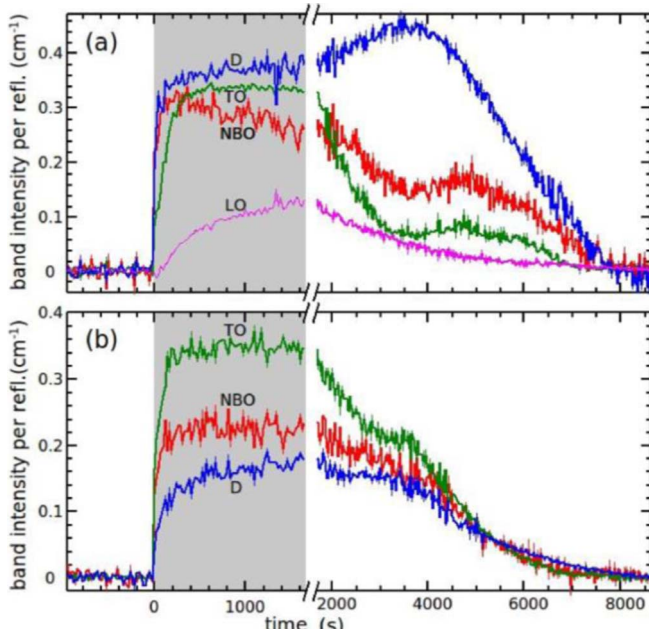


Figure 4. Evolution of the vSiO band intensities as obtained from the fits of the RT spectra. (a) p polarization, and (b) s polarization. The shaded region indicates the time spent at the positive potential. Note the break in the time scale at the time of the negative potential step, and the complex behavior at longer times.

^eAt $t=3000$ s, i.e., 1320 s after the negative-potential step, the relative change in band intensity in p (s) polarization for NBO, TO, D, LO is $\approx -30\%(-20\%)$, $-70\%(-40\%)$, $+15\%(-20\%)$, -50% , respectively.

^fThough the integrated intensities of the whole vSiO band in s polarization and p polarization keep their simple physical meaning, the polarization dependence of the individual component bands can hardly be given a simple interpretation: due to the strong band overlap, the classical simple rules of internal-reflection spectroscopy [typically, p to s absorption ratio $\text{abs}(p)/\text{abs}(s) = (A_x + A_z(n_{\text{water}}/n_{\text{layer}})^4)/A_s$, using the notations of Ref. 10] must be revised. Especially, the bands located in the lower-energy part of the massif exhibit a weakened polarization dependence (NBO, TO; p/s ≈ 1), whereas those located in the higher-energy part of the massif exhibit an enhanced polarization dependence (D; p/s ≈ 2). These figures can indeed be reproduced by numerical simulation of the p-spectra from the s-spectra through a Kramers-Kronig analysis. The presence of a weak maximum of the D band intensity in p polarization during the dissolution, whereas a plateau is observed in s polarization, can be attributed to several (non-exclusive) phenomena. We regard as most plausible the mechanism resulting from a decrease of the refractive index of the layer during the dissolution and the associated increase of the electric-field component normal to the surface in p polarization [the factor $(n_{\text{water}}/n_{\text{layer}})^4$].

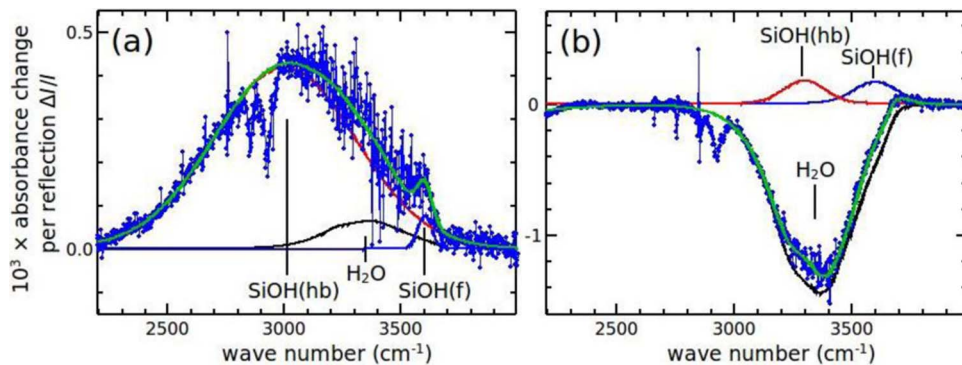


Figure 5. Fits of p-polarized RT spectra in the νOH region: (a) spectrum #41 (just after the positive potential step) and (b) spectrum #110 (just before the negative potential step). Data after baseline subtraction (blue dots), fit (bold green line), water (H_2O), and the two Gaussians [$\text{SiOH}(\text{hb})$ and $\text{SiOH}(\text{f})$], as indicated in the figure. The region $2750\text{--}2980\text{ cm}^{-1}$ (spurious contributions from the O-ring seal) has been excluded from the fit. Note the different scales and the conspicuous change in overall shape between the two spectra, especially the strong predominance of the $\text{SiOH}(\text{hb})$ contribution in (a).

of a strong and very broad band centered at ca 3000 cm^{-1} . This strong variation of the νOH spectrum through the potential cycle has motivated a more quantitative analysis.

Previous studies.—The νOH signals may include i) a contribution from free water of known shape (electrolyte displaced from the IR probing region in the presence of an oxide layer), ii) a contribution from interfacial water, generally centered at a lower energy, as demonstrated by sum-frequency-generation experiments;¹⁷ iii) SiOH contributions, known to consist of isolated SiOH groups at around 3650 cm^{-1} , and SiOH groups in hydrogen-bonding interaction with their environment (water and/or other SiOH groups), appearing as a broader band at a lower energy, a shift that may reach several hundred cm^{-1} .^{18,19} In a previous work on Si in acidic fluoride medium,²⁰ the OH band attributed to SiOH groups was indeed found to have a complex shape: a rather narrow band at around 3640 cm^{-1} , corresponding to “free” SiOH groups, [$\text{SiOH}(\text{f})$], and a broader structure, fitted as the superposition of two Gaussian curves, centered at around $3400\text{--}3500\text{ cm}^{-1}$, and corresponding to hydrogen-bonded SiOH groups [$\text{SiOH}(\text{hb})$].

In the present experiments (6 M KOH electrolyte), free SiOH groups may be present inside the oxide layer, but it is likely that the major part of the surface silanol groups will be ionized and mostly SiO^- (silanolate groups) will be left on the surface. However, a specific contribution from such groups is to be expected, because they will interact with water molecules through hydrogen bonding ($\text{SiO}^- \cdots \text{HOH}$ groups, with the possible involvement of K^+ ions, e.g., $\text{SiO}^- \cdots \text{K}^+ \cdots \text{OH}_2$ or $\text{SiO}^- \cdots \text{HO}[\cdots \text{K}^+] \text{H}$), leading to a change in absorption of the water molecules in the double layer.

Fitting procedure.—Given the above points, we fitted the νOH band by including three vibrational contributions: i) the electrolyte, whose spectral shape is known (1 adjustable parameter), ii) a Gaussian representing $\text{SiOH}(\text{f})$, identified as the highest-energy contribution to the νOH band (ca 3600 cm^{-1}); iii) the remainder (interfacial water and hydrogen-bonded species) was represented by a single Gaussian contribution at a lower energy, and termed for convenience $\text{SiOH}(\text{hb})$ (though this contribution may arise largely from interfacial water, typically in $\text{SiO}^- \cdots \text{HOH}$ groups). An alternative choice would have been to take several Gaussian bands to represent the various species plausibly present at the interface. The choice of a single Gaussian contribution was made in order to limit the number of adjustable parameters. The resulting fits are fair, with confidence intervals of at most a few tens of percent (for more details see Supplementary Material I).

General trends.—The spectral decomposition of the spectra in Fig. 5 is shown superimposed on the data. It turns out that, unlike the results reported in Ref. 20, here the $\text{SiOH}(\text{hb})$ contribution definitely cannot be considered as fixed in shape. The results obtained from the fits are shown in Fig. 6. They must be considered with some

caution, because the number of free parameters is somewhat large, as the noise in the results (Fig. 6) and a visual inspection of Fig. 5b indeed suggest (the confidence limits of some parameters may reach a few tens of percent, see Supplementary Material I). Especially, the

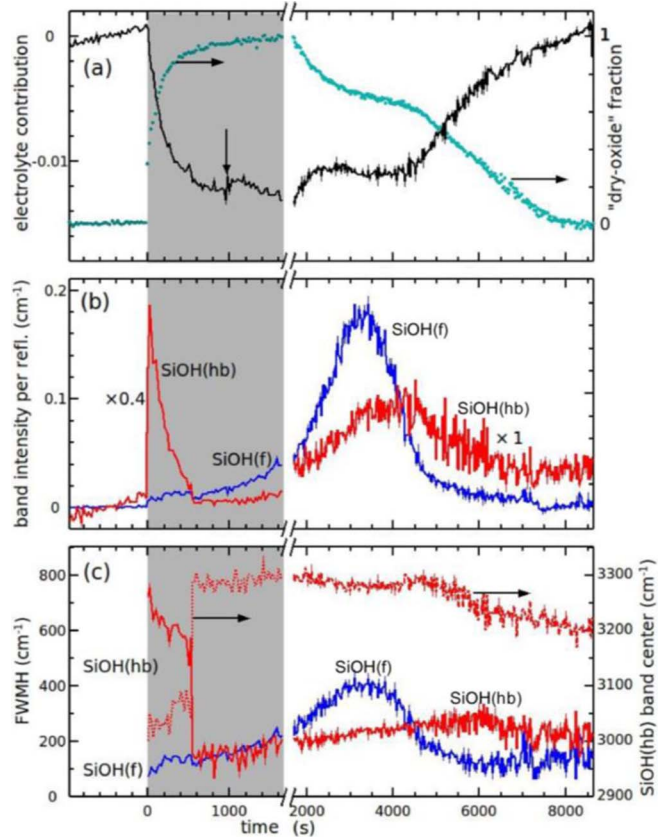


Figure 6. Results from the νOH fits (RT, p polarization). The shaded region indicates the time spent at the positive potential. Note the break in the time scale at the time of the negative potential step. The red (resp. blue) curves refer to the $\text{SiOH}(\text{hb})$ [resp. $\text{SiOH}(\text{f})$] band. Note the steep change in shape [(c): center, dashed red line, and width, solid red line] of the $\text{SiOH}(\text{hb})$ absorption at $t = 550\text{ s}$. The accident at $t = 1000\text{ s}$ (see arrow in the upper left frame) is plausibly due to a small bubble lifting off from the surface. The cyan dots in (a) represent the fraction of “dry oxide”, taken as the sum of the area of the vSiO TO, D and LO bands, normalized to its value before the negative-potential step. Note the negative correlation with electrolyte absorption.

limits of the fitting procedure appear in the fact that the SiOH(hb) band intensity does not return exactly to zero at the end of oxide dissolution (Fig. 6b), which indicates that the baseline is not ideally taken into account. However, a robust result is that, on the anodic potential step, the SiOH(hb) contribution appears as a broad band at a very low wave number (center $3050\text{--}3100\text{ cm}^{-1}$, FWHM $600\text{--}700\text{ cm}^{-1}$, see Fig. 5a), and it is only after some oxide has grown that its position and width become more in line with the data of Ref. 20 (here position at ca 3300 cm^{-1} , FWHM $150\text{--}250\text{ cm}^{-1}$, see Fig. 5b). This change in shape occurs rather suddenly around $t = 550\text{ s}$, which suggests that the two shapes correspond to two distinct species, and a better fit might be obtained by adding an extra Gaussian component. However, we have not done that, because the parameters of the two bands appear to vary with time, and a three-Gaussian fit would lead to an unreasonably large number of adjustable parameters.

Salient features.—The fits clearly indicate that i) there is a negative correlation between the electrolyte contribution and the total amount of “dry oxide” (see Fig. 6a), as may be expected from the oxide-exclusion mechanism, ii) at the beginning of the oxidation, and also to a lesser extent in the later stage of oxide dissolution (Fig. 6b), the evolution of the shape of the SiOH(hb) contribution (larger FWHM and lower energy of the center) indicates the presence of a contribution on the low-energy side, a robust result indeed independent of the detail of the fit, iii) there is a transient increase in the SiOH(f) + SiOH(hb) contribution (together with a delay in the recovery of excluded water) during the dissolution (Figs. 6b and 6a).

Miscellaneous vibrational bands.—In addition to the above bands, all of the spectra exhibit a number of weaker vibrational signals, especially the water scissor mode δOH_2 at 1640 cm^{-1} . From the fits, it appears that, as it was to be expected, this band behaves in the same way as the electrolyte vOH contribution, namely it exhibits a negative correlation with the oxide contribution (oxide-exclusion mechanism).^g

The 40°C study.—The 40°C results appear surprisingly different from the RT results. As was to be expected, the time scale on which the changes take place is much shorter. However, the most conspicuous change is in the shape and magnitude of the baseline, which was shown to be due to hydrogen incorporation into the Si lattice at the negative potential.⁵ The magnitude of this baseline makes the analysis of the vibrational regions more difficult than for the RT data, and the results obtained are less accurate (confidence limits may reach a few tens of percent, see Supplementary Material I).

vSiO region.—The fit of the vSiO spectrum has been performed in the ($880\text{--}1360\text{ cm}^{-1}$) window, as the superposition of four Gaussian bands (three for s polarization), plus a background as described in the Appendix, Sec. II. The observed behavior is essentially similar to that found for the room-temperature data: on the positive-potential step, the NBO mode (940 cm^{-1}) is present from the very first spectrum, and the LO mode (1180 cm^{-1}) appears last (Fig. 7). On the negative potential step, the TO and LO modes drop in intensity and fully disappear after 300 s, whereas the NBO and D band intensities decay less rapidly (the very long tailing-off of the D band intensity for the p polarization may actually be due to an imperfect fitting of the background).^h As was to be expected, oxide dissolution is seen to be

^gOther conspicuous bands are vCH at 2855 and 2930 cm^{-1} (see Figs. 2c and 5), and other features at 1400 and 1550 cm^{-1} (stronger). All of these features originate from the fluoroelastomer O-ring seal used to mount the sample on the cell.⁵ In principle O-ring seal absorption is not expected to appear in the differential spectra. However, the magnitude of these features is found to behave in the same way as those of the electrolyte vOH and δOH_2 contributions (negative correlation with the oxide contribution). This observation indicates that anodic oxidation takes place under the seal by water creeping, and O-ring seal absorption is screened by the oxide layer, just in the same way as electrolyte absorption. Such a phenomenon does not appear in the 40°C data, possibly due to a temperature change in the wetting and rheologic properties of the elastomer.

^hAt $t = 1000\text{ s}$ (100 s after the negative-potential step), the relative change in band intensity in p (s) polarization for NBO, TO, D, LO is $\approx -20\% (+10\%)$, $-30\% (-35\%)$, $-10\% (+5\%)$, -60% , respectively.

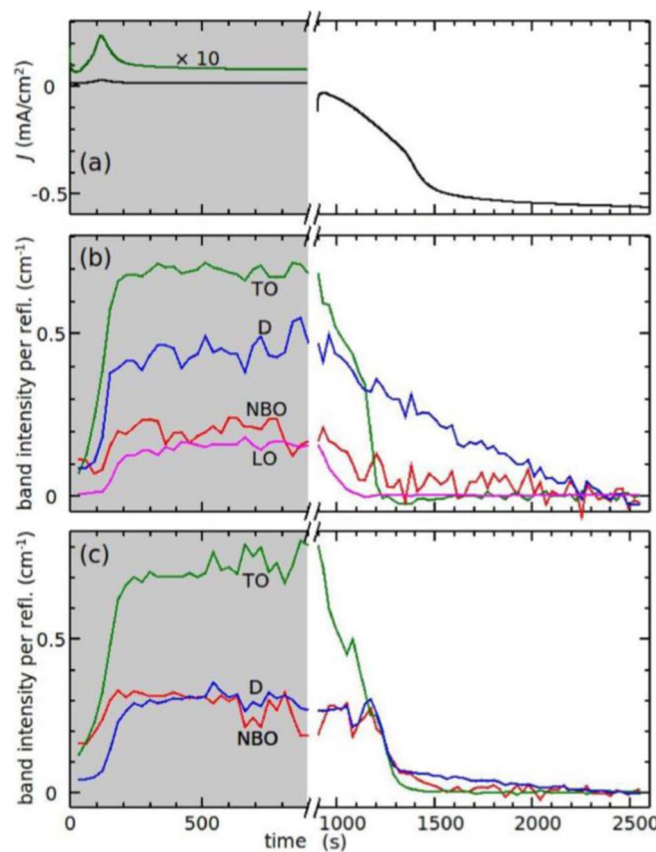


Figure 7. 40°C data. (a) Current transients. (b-c) Results of the fits of the vSiO region: (b) p polarization and (c) s polarization. The shaded region indicates the time spent at the positive potential. Note the break in the time scale at the time of the negative potential step ($t = 900\text{ s}$).

faster at 40°C than at RT. Also, the initial intensity transfer from TO and LO to NBO and D seems somewhat weaker at 40°C than at RT. However, the overall behavior of oxide dissolution at 40°C appears in line with the RT data.

Apart from the shorter time scale for oxide dissolution, the most striking difference with the RT data is that the oxide layer appears to reach its steady state 200 s after the positive-potential step (no increase at longer times), but its formation begins after an induction time (see small amount of oxide in the first spectrum, most of the growth of the four Gaussian bands taking place between $t = 50$ and 200 s). Such an induction time was not obvious at RT.

Electrolyte bands.—A first attempt at fitting the electrolyte bands (vOH and δOH_2) as a superposition of electrolyte absorption and a second-order polynomial background was unsuccessful. It appeared that a good fit required an additional component proportional to the real part of the optical index of the electrolyte. This strange behavior can be attributed to the large magnitude of the background, and to the appearance of a cross effect between baseline absorption and electrolyte absorption (see Supplementary Material II: Cross effect between baseline absorption and electrolyte bands).^{21,22} We have been able to reproduce this type of spectrum by numerical simulations, using the assumption that an interlayer is present at the interface. This interlayer was described, in the framework of the Bruggeman effective-medium approximation,²³ as a mixture of “modified silicon” (silicon with centers responsible for the baseline absorption) and electrolyte.²⁴ The success of this analysis adds further support to our interpretation of the baseline absorption.⁵ Unfortunately, the presence of this unwanted effect makes it very difficult to extract

useful information on the surface chemistry from the νOH and δOH_2 spectra.

Discussion

We will now compare and discuss the results of the RT and 40°C experiments. The mechanisms of oxide formation at the positive potential and oxide dissolution at the negative potential will be addressed successively.

Mechanism of oxide formation.—The νSiH and νSiO data provide complementary evidence that the positive potential step leads to a loss of the surface (and sub-surface) hydrogen, followed by the appearance of an oxide layer. A common feature of the RT (Figs. 4, 6) and 40°C (Fig. 7) data is the fact that the oxide appears first in the form of the non-bridging oxygens (NBO) and the so-called “disorder” (D) bands. Note that the latter band may actually include isolated siloxane bridges at the beginning of oxide formation. From the analysis of the νOH region in the RT data, it appears that different types of NBO sites are involved in the oxidation process. The strong and broad low-energy OH band, at around 3000 cm^{-1} , present at small oxide coverage, may be assigned to silanolate ($\equiv\text{Si}-\text{O}^-\cdots\text{H}-\text{O}-\text{H}$) groups at the surface of silicon (the large energy shift and broadening indicating a strong hydrogen bonding, usually associated with a huge increase of the optical cross-section¹⁸). At higher oxide coverage, NBO sites are either silanols (inside the oxide) or silanlates (at the oxide surface), as evidenced by the higher-energy OH bands ($3600\text{--}3300\text{ cm}^{-1}$, Fig. 5). These attributions are further supported by the fact that the pK_a of a silanol at the surface of silica is around 8.5,²⁵ whereas that of trialkylsilanols (expected to be close to the pK_a of a silanol at a silicon surface) is in the range 12–14;^{26–28} hence, the softening of the water-OH frequency in a $\equiv\text{Si}-\text{O}^-\cdots\text{H}-\text{O}-\text{H}$ complex in concentrated KOH solution is expected to be more pronounced for a silanolate at the surface of silicon than for one at the surface of silica. Also, the broad low-energy contribution may result from the presence of NBO sites at the silicon surface through another (non exclusive) mechanism: since the pK_a value of a silanol at the silicon surface may approach 14 and titration curves are known to be significantly broadened at surfaces,²⁹ it is likely that a non-negligible number of silanol groups (i.e., in the protonated form) will survive at the silicon surface even in our experimental conditions. The νOH vibrations of SiOH groups are expected to be lower in energy by about 100 cm^{-1} with respect to those of the water molecules to which they are H-bonded,³⁰ which accounts for the experimental shifting and broadening of the SiOH(hb) contribution on the low-energy side.

The well-defined oxide layer appears with some delay, as seen by the rise of the TO and LO bands (Figs. 4 and 7). From the intensity of the νSiO bands, and following the method of Ref. 11, the steady-state oxide thickness at the positive potential is estimated to be 1.14 nm at RT. From the intensity of the excluded water signal (Fig. 6a), an effective thickness of 1.4 nm is obtained. These two estimates can be regarded as consistent.ⁱ For the 40°C data, only the νSiO data are available, and lead to a value of 1.7 nm, i.e., ~50% higher than at RT. These figures can be compared to faradaic estimates based on the integration of the anodic current transient. Note that the latter method suffers from an uncertainty in defining a baseline before performing the summation. The results obtained, based on the equivalence 1 nm $\text{SiO}_2 = 1.4 \text{ mC/cm}^2$ (tetravalent dissolution and specific gravity of silica of 2.2 g/cm^3), do not exhibit a significant difference between RT and 40°C, and fall in the range 1.1–1.8 nm, in reasonable agreement with the results from IR.

ⁱAn anodic oxide is not as compact as a dry oxide, hence, the νSiO band intensity leads to an underestimate, whereas the value from electrolyte exclusion may be an overestimate, because the presence of the oxide (and the associated silanolate species) is likely to perturb absorption of the electrolyte in the double layer through hydrogen-bonding interactions. The observed mismatch between the two estimates (0.3 nm) is fairly consistent with the latter mechanism (perturbed zone = 1–2 ML of water molecules).

As noted above, the most striking difference between the RT and 40°C data concerns the first steps of oxide formation, which can now be compared with the current transients and νSiH data.⁵ At RT, though a steady state is reached only after ca 1000 s, there is an important initial anodic current spike, most of the SiH termination is lost in the first 30 s after the positive potential step (see Ref. 5 and Section *Simulation of oxide formation* below), and the NBO and D bands appear simultaneously. At 40°C, counter-intuitively, the anodic current transient is *delayed* (maximum at 120 s), and the loss of SiH and appearance of oxide bands are more gradual, extending over a duration of ca 150 s. An attempt at understanding this puzzling behavior will be presented after consideration of the oxide-dissolution data.

Mechanism of oxide dissolution.—Figs. 3, 4, 7 indicate that the properties of the oxide change during its dissolution: the initial persistence of the D and NBO bands (and even a slight increase of the D band in Fig. 4a), at the expense of the TO and LO bands, indicates a loss in “quality” of the oxide. For the RT data, this is further supported by the transient variation of the silanol bands at 3300 and 3600 cm^{-1} : the intensities and widths of the two bands go through a maximum, the variations of the SiOH(f) band preceding those of the SiOH(hb) band (Fig. 6). The variation of the widths suggests that a broad distribution of H-bonding strengths is present (the so-called SiOH(f) band actually including weakly—possibly sterically hindered—H-bonded sites), and the mean H-bonding strength increases with time, suggesting a progressive penetration of water into the oxide. A plausible scenario is that dissolution is initiated by penetration of OH^- ions into the oxide, followed by breaking of siloxane bridges according to the reaction $\equiv\text{Si}-\text{O}-\text{Si}\equiv + \text{OH}^- \rightarrow \equiv\text{Si}-\text{O}^- + \text{HO}-\text{Si}\equiv$, leading to the growth of the SiOH(f) band. When these sites are reached by water molecules, the SiOH(f) band decreases while the SiOH(hb) band in turn grows. Recovery of a hydrogenated surface starts after some delay (3000 s at RT, 300 s at 40°C) and is very gradual.⁵ Noticeably, in the dissolution regime (and unlike what is observed during oxide formation), the p/s ratio of the various bands significantly deviates from the constant value that would naively be expected ($\text{p/s} \approx 1$ for TO, ≈ 1.5 for NBO and D, infinite for LO). While the latter feature can hardly be discussed quantitatively (see footnote f in the Results section), these apparently complex trends may be understood in terms of a random dissolution process. As shown schematically in Fig. 8a: i) random dissolution (i.e., with equal probability of dissolution of any surface site) is expected to lead to a porous oxide (the lowered optical index, possibly together with anisotropy effects, accounting for the increase in the p/s ratios), ii) as compared to the behavior expected from a layer-by-layer dissolution process, the recovery of the hydrogenated surface is expected to start after a shorter induction time, but iii) it is expected to progress at a more gradual rate, since total recovery is obtained only after complete dissolution of the oxide.

Simulation of oxide dissolution.—We have attempted a more quantitative verification of the above idea through numerical simulations. The dissolution process lends itself easily to a direct Monte Carlo simulation. The oxide layer was represented by a set of sites on a simple cubic lattice. As a first step, we assumed that any surface site may be dissolved with equal probability per unit time k_d (see scheme Fig. 8a). The actual simulation was performed on a 50×50 grid, and the initial oxide thickness was varied from 1 to 7 ML. At each step of the simulation, the surface sites (in contact with the electrolyte) were listed and one of them was randomly selected and removed. The dimensionless time $k_d t$ was then incremented by $1/N_s$, where N_s stands for the number of surface sites. The results are shown as Figs. 8b–8c. They reproduce the features observed experimentally, namely, a delay in the appearance of the hydrogenated surface and a spread in the recovery time. Also, the oxide dissolution rate, which is initially equal to 1 (in units of $\text{ML} \times k_d$) is seen to increase after an induction time on the order of k_d^{-1} , an effect attributable to the increase in specific surface area of the oxide during its dissolution. However, the simulated variations of the remaining oxide fraction and

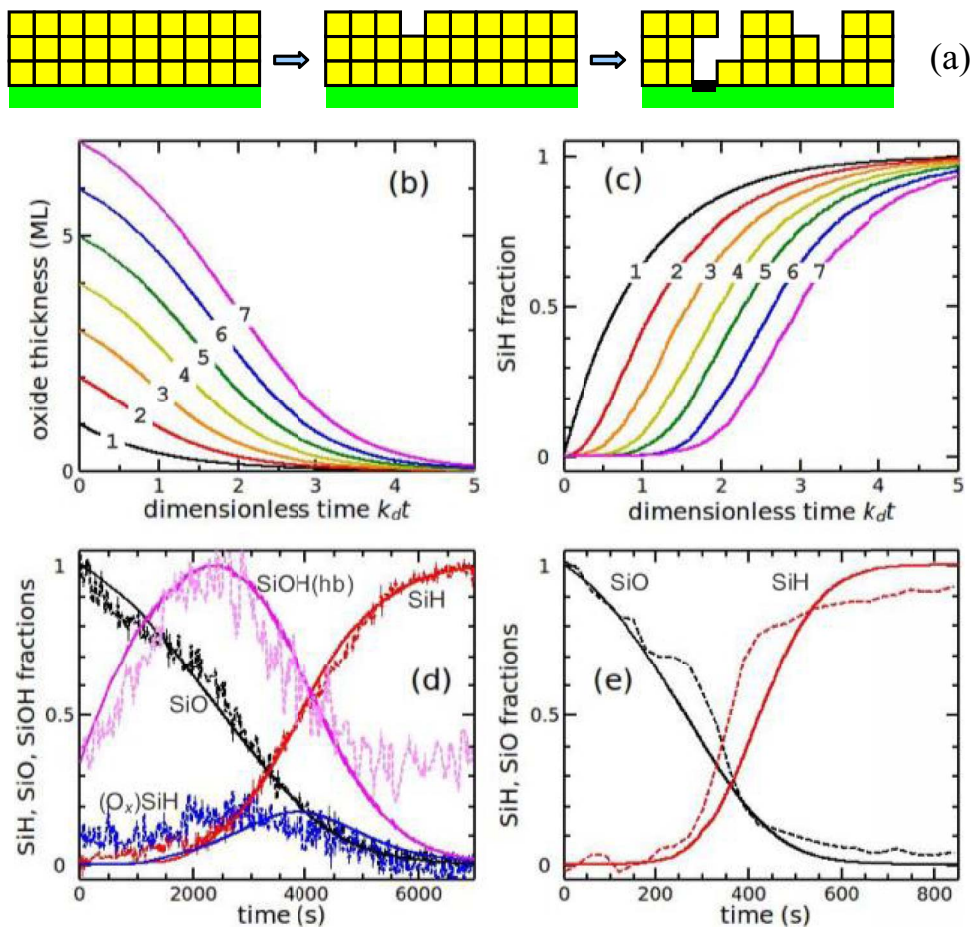


Figure 8. Simulations of oxide dissolution. (a) Principle of the simulation (here 2D scheme starting from a thickness of 3 ML). (b-c) Results of 3D simulations on a 50×50 sample, when starting from 1 to 7 ML (see labels on the curves). (b) Oxide thickness and (c) fraction of hydrogenated surface as a function of reduced time k_{dt} (here $k_d = \text{constant}$). (d-e) Comparison with the experimental results: SiO fraction (referred to the initial state), unoxidized SiH fraction (referred to the final state, experimental data from Ref. 5), SiOH(hb) fraction, obtained from the oxide area in contact with the electrolyte (referred to its maximum) and SiH with oxidized backbonds (referred to the final unoxidized SiH, experimental data from Ref. 5). Experimental data (dashed noisy lines) and results from the simulations (solid smooth lines), here with $k_d = k_0 \alpha^{(n_{el}-1)}$ and $\alpha = 1.5$. (d) RT results, with $k_0 = 0.0004 \text{ s}^{-1}$ (the solid line for $(O_x)\text{SiH}$ is the time derivative of the simulated SiH fraction, multiplied by 500 s). (e) 40°C results, with $k_0 = 0.005 \text{ s}^{-1}$.

hydrogenated surface fraction appear to tail-off at long times somewhat more markedly than for the experimental data. This mismatch may be corrected by assuming that the dissolution probability of an oxide site is actually a function of the number n_{el} of its electrolyte nearest neighbors. The technical problem of using a weighted probability was dealt with as is done classically.^{31,32} At each step of the simulation, the sum $S_0 = \sum_{i,j,l} k_d(i,j,l)$ was calculated (sum extended to the N_s surface sites), the time was incremented by $1/S_0$, and a random number S was selected, with a flat probability distribution between 0 and S_0 . The site (i_0, j_0, l_0) to be dissolved was determined by ordering the subset (i, j, l) of surface sites through the use of a single index m and selecting $m_0 = \min(m) | [\sum_{m'=1}^{m'-m} k_d(m') > S]$. Since each surface site is represented in the sum S_0 with a weight given by its specific dissolution probability, this procedure respects the k_d hierarchy, that is, sites with a higher k_d have a higher probability of being selected. Choosing a simple exponential-like assumption

$$k_d = k_0 \alpha^{(n_{el}-1)}, \quad [1]$$

where k_0 is the dissolution rate at a flat surface, and using $\alpha = 1.5$, the simulation is seen to agree nicely with the experimental data (Figs. 8d–8e).

The initial thickness was taken as 4 ML for the RT data (i.e., 1.2 nm on the basis 1 ML = 0.3 nm), and 6 ML (1.8 nm) for the 40°C

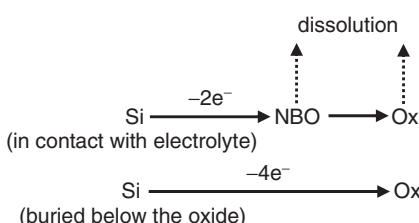
data. k_0 was used as the only adjustable parameter and was found to be 0.0004 s^{-1} for the RT data, and 0.005 s^{-1} for the 40°C data. The SiO and SiH fractions are seen to match the experimental results, especially for the RT data, which involve lower experimental uncertainties than the 40°C data. The minor deviations at the beginning of the dissolution may be attributed to the initial roughness, not taken into account in the simulation. Interestingly, the surface area exposed to the electrolyte [obtained from $\Sigma n_{el}(i,j,l)$, pink line in Fig. 8d] exhibits a variation closely similar to that found experimentally for the SiOH(hb) contribution. Also, the derivative of the SiH fraction exhibits a maximum similar to that observed for the intensity of the SiH(2120) band corresponding to SiH with oxidized Si backbonds. This was indeed to be expected, because SiH groups with oxidized backbonds must be present as a transient state in the final stage of oxide dissolution.

The fair agreement of the simulation results with experiment clearly supports the idea that dissolution takes place in a random manner, creating a porous oxide as a transient state. This idea receives still further support from the change in shape of the vSiO spectrum during the dissolution. As is shown in Supplementary Material III (IR absorption of a porous oxide layer), the appearance of a broad contribution located between the TO and LO modes is expected for a porous material in thin-layer form, including for thicknesses on the order of a monolayer. This prediction matches the experimental observation of a transient persistence (or increase) of the D band. Note

that this behavior lasts up to about the same time as the reappearance of the surface SiH groups,⁵ i.e., the time at which the oxide has become porous down to the silicon surface. A somewhat better fit of the oxide dissolution curve for the 40°C data would be obtained with a higher value of α , which suggests that the porous fraction of the oxide layer is smaller at 40°C than at RT (consistent with the weaker intensity transfer from TO and LO to NBO and D). However, this change in α leads to a worse fit of the SiH recovery curve, a problem due plausibly to hydrogen insertion into the Si lattice.⁵ We have chosen to ignore these complex phenomena, and we have kept α constant in the simulations. Though the detail of the variation of the four bands might deserve further consideration, it can be concluded that we have reached a satisfactory level of understanding of the oxide dissolution mechanism.

Simulation of oxide formation.—A simulation of oxide formation was attempted along the same lines as that of oxide dissolution, and using the same algorithm for the simulation of events with distinct probabilities per unit time. However, oxide formation is a much more complex process than oxide dissolution, because oxidation at the silicon surface and dissolution at the outer oxide surface take place simultaneously. Furthermore, oxidation of a hydrogenated silicon surface site leads to an NBO site (SiOH or SiO^- group), and *bona fide* oxide can be obtained only after condensation of such groups,³³ or by oxidation of “buried” silicon atoms (not in direct contact with the electrolyte). For the sake of simplicity, we deliberately kept our simple-cubic-lattice model (in which each site may now represent silicon, electrolyte, oxide, or NBO). Even in this very simplified framework, the surface silicon sites to be oxidized may have a variety of different environments (n_{el} electrolyte neighbors, n_{ox} oxide neighbors, and n_{NBO} NBO neighbors, and implicitly $6 - (n_{\text{el}} + n_{\text{ox}} + n_{\text{NBO}})$ silicon neighbors, with $n_{\text{el}} + n_{\text{ox}} + n_{\text{NBO}}$ varying from 1 to 6!). Finally, the kinetics may be limited not only by the local environment of the site being oxidized, but also by the mass-transport mechanisms in the oxide and the supply of electric charge. At first sight, it may appear surprising indeed that significant anodic current densities are observed at an n-type electrode in the dark (i.e., in the absence of hole supply). The origin of the large anodic current observed may be understood in terms of electron transfer to n-Si mediated by surface states associated with the oxidation process^{34–39} (at high pH, the barrier for electron injection from such states to the conduction band is only of a few hundred millivolts). In the following, we will assume that charge transfer is not a limitation and that the kinetics are simply ruled by the local environment of the sites being oxidized.

In a pioneering study, Smith et al. invoked the transformation of a “chemical oxide” to “anodic oxide” as the origin of the first contribution to the anodic current transient, the second contribution corresponding to the nucleation and growth of oxide islands.⁹ Though the initial state of the surface is actually hydrogenated, we have retained the idea of a two-step mechanism, the first step now consisting in the oxidation of SiH groups to NBO sites, and the second step being similar to that proposed by Smith et al., leading to the mechanism summarized in Scheme I. Note that this model implies that there is no direct silicon dissolution channel, i.e., dissolution proceeds solely through oxide formation / oxide dissolution. As is generally agreed,^{40,41} the charge associated with oxidation of a silicon site with $n_{\text{el}} = 0$ was taken as $4e$, and that associated with oxidation of a site with $n_{\text{el}} > 0$



Scheme I. Summary of the oxide formation mechanism.

was taken as $2e$. It was assumed that the different reaction probabilities depend on the environment according to power laws (a simple one-parameter parametrization of a dependence on the neighborhood), as it was done for the simpler case of oxide dissolution.

- Anodic steps were assumed to be governed by the local environment, and not by the semiconducting character of the electrode (see above):

-Formation of NBO sites was assigned a probability k_{NBO} taken as

$$k_{\text{NBO}} = k_1 \beta^{(n_{\text{el}} - 1)} \gamma^{n_{\text{NBO}}} \quad \text{if } n_{\text{el}} > 0 \text{ (otherwise } k_{\text{NBO}} = 0\text{)}, \quad [2]$$

where k_1 is a prefactor and the parameters β and γ describe the effect of the environment (number of electrolyte and NBO neighbors, respectively) on the reaction rate.

- In the same spirit, direct oxidation of buried silicon sites ($n_{\text{el}} = 0$) was assigned a probability k_{ox} taken as

$$k_{\text{ox}} = k_3 \epsilon^{(n_{\text{ox}} + n_{\text{NBO}} - 1)} f(d) \quad [3]$$

if $n_{\text{el}} = 0$ and $n_{\text{ox}} + n_{\text{NBO}} > 0$ (otherwise $k_{\text{ox}} = 0$),

where k_3 is a prefactor and d is the distance from the silicon site under consideration to the nearest electrolyte site. The function $f(d)$ describes the effect of oxide thickness on the oxidation rate of buried silicon sites. This rate may be limited either by local kinetics or by the transfer of ionic species through the oxide, which is expected to be a sharply varying function of d ; hence, the shape of a smoothed step function centered around a critical value d_c is plausible. In practice we chose the form: $f(d) = 1/[1 + \exp((d - d_c)/w)]$, where w is a characteristic length plausibly smaller than d_c (k_3 describes the limitation by local kinetics, while d_c and w arise from the limitation by mass transport through the oxide).

- Condensation of NBO sites to oxide sites was assigned a probability k_{cond} taken as

$$k_{\text{cond}} = k_2 n_{\text{NBO}} \delta^{(n_{\text{ox}} + n_{\text{NBO}} - 1)} \quad \text{if } n_{\text{ox}} + n_{\text{NBO}} > 0 \text{ (otherwise } k_{\text{cond}} = 0\text{)}, \quad [4]$$

where k_2 is a prefactor and δ describes the effect of the environment.

- Oxide-site dissolution was assigned the same probability law as above [Eq. 1].

• NBO-site dissolution was assumed to follow a similar law as oxide-site dissolution, though with distinct values of the parameters:

$$k'_d = k'_0 \alpha^{(n_{\text{el}} - 1)} \quad \text{if } n_{\text{el}} > 0 \text{ (otherwise } k'_d = 0\text{)}. \quad [5]$$

The parameter β , which describes the anisotropy of the oxidation process (faster kinetics for protruding sites), is expected to be larger than 1. After varying the parameters for mimicking the experimental data, and though the resulting values bear an important uncertainty, we found that δ and ϵ are also larger than 1 (sites close to oxidized ones are more easily oxidized), but it appears that γ may be either larger or smaller than 1. Values $\gamma < 1$ may be due to the electrostatic repulsion between neighboring SiO^- groups (if electrostatic screening is not sufficient, it may be more difficult to create an SiO^- in the vicinity of a pre-existing one). These simulations reproduced the current maximum but not the initial current spike. The latter feature was reproduced by allowing a few (typically 4) monolayers of Si to dissolve chemically before oxide formation begins (random dissolution with a rate $\propto \alpha'^{(n_{\text{el}} - 1)}$; since the number of monolayers to be dissolved is specified, the rate prefactor is unimportant). The atomic steps generated by this process do lead to a large initial current, which decreases rapidly upon passivation of these sites. Figure 9 shows the results of a simulation compared with experiment. Table II shows the parameters used, whose values were determined by a random try-and-see algorithm (a conventional least-square approach is not easy to implement here, due to the stochastic character of the model). Though these two sets may not represent the optimum parameters, the agreement is satisfying.

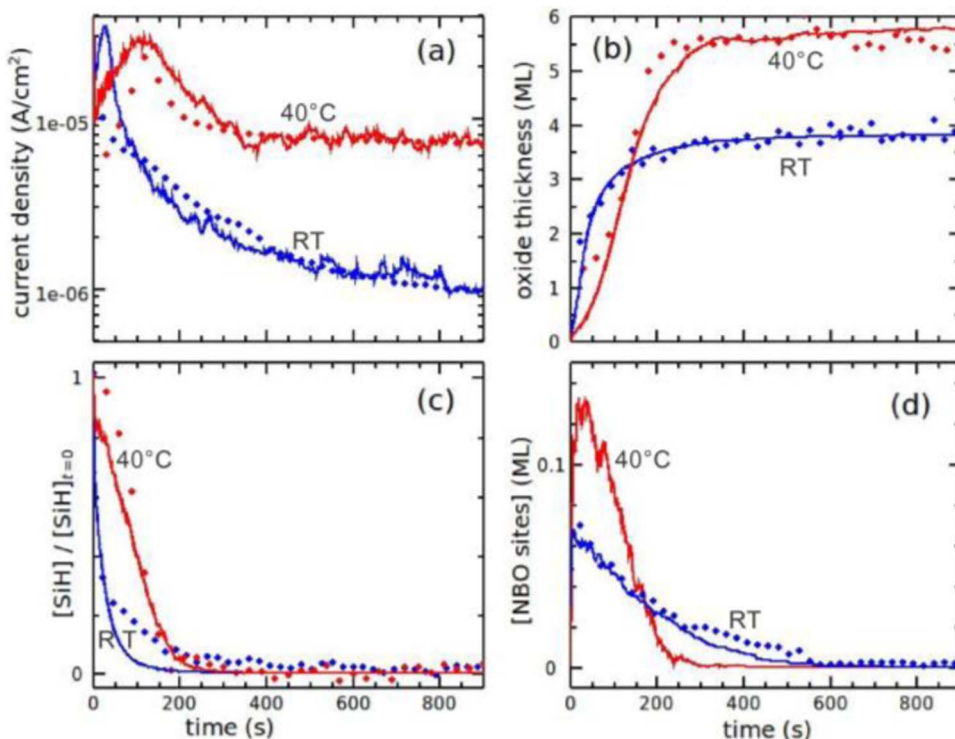


Figure 9. Results of the simulations of oxide formation on a 50×50 sample (lines) compared to experiment (dots). (a) Current density, (b) oxide thickness, (c) fraction of hydrogenated surface, (d) fraction of NBO sites compared to the scaled SiOH(hb) signal (RT data only), as a function of time. Note that the experimental data for SiOH(hb) involve silanolate groups at the surface of SiO_2 , which are not taken into account in the simulation.

Table II. Parameters for the simulations of oxide formation (all k 's are given in units of s^{-1} , d_c and w in units of $\text{ML} = 0.3 \text{ nm}$). For each parameter, the first line gives the value at RT, and the second line the value at 40°C.

Reaction parameters							
Oxide dissolution [reaction 1]	k_0	0.00027	α	4.4			
		0.0033		1.6			
NBO dissolution [reaction 5]	k'_0	0.0078	α'	1.1			
		0.042		2.9			
NBO formation [reaction 2]	k_1	0.017	β	9.1	γ	2.7	
		0.011		13.		0.13	
NBO condensation [reaction 4]	k_2	0.58	δ	18.			
		0.089		1.7			
Direct oxidation [reaction 3]	k_3	0.019	ϵ	2.2	d_c	2.4	w
		0.013		1.5		4.1	0.15
Preroughening parameter			α''	16.			
				22.			

One can check that the values found for k_0 essentially agree with those obtained from the dissolution simulations.^j Interestingly, the puzzling differences between the RT and 40°C experiments can be reproduced by these simulations. From Table II, it appears that for the two temperatures many parameters have the same value (within a factor of 2), and we may consider them as essentially temperature independent. Such is the case for most of the dimensionless exponents, and for the rate parameters related to the electrochemical processes (k_1 , k_3), which is not too surprising. The temperature dependence of the oxide and NBO chemical dissolution parameters k_0 and k'_0 (in-

crease by an order of magnitude from RT to 40°C) is consistent with the activation energy of $\sim 100 \text{ kJ/mol}$ reported for the dissolution rate of silica in NaOH solution.⁴² This increase is accompanied by a strong decrease of k_2 (NBO condensation rate). Though the determination of the various exponents bears a large uncertainty, the marked decrease of γ and δ from RT to 40°C appears significant. This variation, together with that of k_2 , may be tentatively attributed to a less efficient screening of the repulsive coulomb interaction between two neighboring silanolate groups at 40°C. To conclude, the delay before passivation is longer at 40°C than at RT, due to the competition between NBO-site formation, dissolution, and condensation. At RT, most of the created NBO sites act as nuclei for oxide formation, whereas at 40°C fast dissolution of many of them occurs before condensation can take place, an effect possibly reinforced by a lowering of the condensation rate at 40°C.

Effect of steps and anisotropy on the current transients.—Finally, as an exploratory investigation of the anisotropic effects, the simulations can be extended to the case of surfaces obtained by cutting the simple-cubic lattice at an angle from the xy -plane direction. Figure 10 shows the comparison of the current transients for four simulations obtained for different initial surfaces. The black line (a) represents a simulation starting from an ideally flat xy surface, which consists of sites with $n_{\text{el}} = 1$ (mimicking a (111) Si surface), using the same parameters as listed in Table II (40°C parameters). The dotted gray line (b) shows the effect of the pre-dissolution of 4 atomic layers with $\alpha'' = 22$ (similar to the results presented in Fig. 9). Note the initial current peak associated with the higher dissolution rate of the step and kink sites ($n_{\text{el}} = 2$ and 3). The blue line (c) shows the result obtained from the same parameter set for a surface tilted by 45° along the x and y directions, which consists of sites with $n_{\text{el}} = 3$ (mimicking a (100) or (110) Si surface). The initial current density is much larger, and the overall shape of the transient becomes very similar to that of the transient at a (100) surface (see Fig. 1). However, in contrast to experiment, a non-monotonic shape of the transient is obtained.

^jThe ~ 30 percent difference between the two values could be made weaker by finely tuning the thickness taken for the definition of a monolayer (which was taken here as 0.3 nm; a value of 0.36 nm, corresponding to the size of a cube containing an elementary SiO_2 unit, might be more appropriate). Given the semi-quantitative character of these simulations, we have not gone into such refinements.

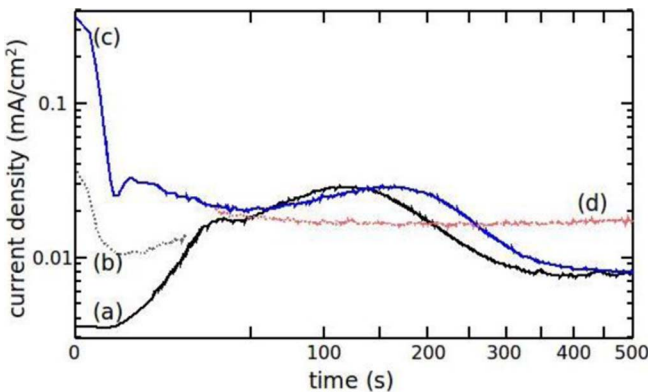


Figure 10. Comparison of the anodic current transients obtained from simulations on (a) an ideally flat xy surface, (b) a slightly roughened surface, and (c) a surface tilted by 45° along the x and y directions, using the parameters of Table II (40°C). The simulation for (d) is similar to that for (c) with modified parameters for reaction 3 ($d_c = 3 \text{ ML}$, $w = 2 \text{ ML}$). The curves represent the filtered average of 10 simulations. Time has been plotted on a square-root scale to better show the short times. Curve (b) nearly coincides with (a) for times $t > 20 \text{ s}$ (not represented for clarity) and (d) is close to (c) for $t < 30 \text{ s}$ (not represented for clarity). Note the similarity of (a) and (d) with the curves of Fig. 1.

Changing some parameters (e.g., d_c and w , see dotted red line (d)) improves the agreement with experiment. However, the need for such adjustments clearly shows the limits of our simple simulations, which ignore the actual topology of the silicon lattice and of the amorphous silica network (incidentally, this neglect implies that the presence of silicon atoms in a formal valence state between (I) and (III) at the Si/SiO₂ boundary is hardly taken into account). A realistic simulation should take into account the actual structure of the silicon lattice, which plausibly leads to different condensation rates depending on the relative configurations of two nearby silanolates on the (111), (100) and (110) surfaces.³³ It would also require a realistic description of the oxide, with values for the interatomic distances, bond angles, and other parameters (concentration of vacancies, defects, ...) affecting mass transport through the oxide. Such an approach is much more difficult and beyond the scope of this work.

Conclusions

From a detailed analysis of our IR results, and with the help of numerical simulations, we reach a comprehensive picture of the behavior of the n-Si/6 M KOH interface during square-wave potential cycling between -1.3 and $+1 \text{ V}$ vs MSE: i) At the negative potential, oxide dissolution takes place essentially at random, which leads to a porous oxide layer as a transient state, even though the low-coordination surface sites undergo a somewhat faster dissolution; this random dissolution process leads to an increased surface area (higher number of SiOH/SiO⁻ species at the oxide surface) and a speeding up of the dissolution after an induction time; ii) during oxide formation at the positive potential, the initial current peak can be attributed to an initial microroughness of the surface; iii) all the experimental trends are accounted for by a two-step oxide formation mechanism, in which the hydrogenated surface sites are first transformed into NBO sites, which then condense, leading to *bona fide* oxide; iv) the delay observed before the appearance of oxide after the positive potential is applied can be attributed to a competition between dissolution and condensation of the NBO sites, the dissolution being favored at higher temperature, which leads to an increased delay at 40°C ; v) this formation mechanism allows one to explain, at least qualitatively, the current transients measured for different crystalline orientations of the substrate.

Acknowledgments

The authors are indebted to Dr D. Aureau, from Université de Versailles-St Quentin en Yvelines, for kindly checking for the absence of metal contamination on our samples by XPS. One of us (HGGP) thanks the Dutch Technology Foundation (STW, TPC-5990) for supporting his stay at Ecole Polytechnique.

Appendix: Details of the Fitting Procedures Used in this Work:

I - General principles.—Our fitting software allows one to fit the spectra in a given spectral window (possibly excluding some intervals within this window), as the linear superposition of i) several pseudo-Voigt functions simulating the vibrational bands (up to 4 adjustable parameters each), ii) a smooth polynomial baseline (typically constant, linear or quadratic), iii) and several “component spectra” recorded independently in the same window (1 adjustable parameter each). It uses the classical Levenberg-Marquardt non-linear least-square fitting algorithm.⁴³ The quality of the fits is quantitatively assessed through examination of the residuals and of the 2-sigma (95%) confidence intervals and correlations between parameters obtained from the covariance matrix using χ^2 estimate.⁴³ Though this software might allow one to fit the whole spectral range in a single operation, the results here were found to be very sensitive to the fitting of the baseline (quite important in these experiments), and more reliable and reproducible results on the vibrational bands were obtained by fitting them in a restricted spectral range with a “local” baseline, the “full-range” baseline being fitted separately by excluding the regions where vibrational bands are present.⁵ The possibility to include component spectra as inputs to the fit was especially helpful in three instances: i) to represent the loss in electrolyte absorption associated with oxide film growth (electrolyte absorption used as a component spectrum), ii) to fit the free-carrier (FC) absorption (see Ref. 5), iii) to correct for problems associated with detector non-linearity (see below).

Unwanted effects of detector non-linearity and how to take care of this problem.—Fourier-transform spectroscopy is based on the assumption of detector linearity (the electric signal associated with the superposition of beams A and B is just the sum of the signals associated with A and B measured separately). This assumption is reasonably well verified for photovoltaic detectors, especially if a positive electronic feedback is used to compensate for the series resistance of the detector.⁴⁴ Also, various software corrections have been proposed,⁴⁵⁻⁴⁸ some of which are often implemented in commercial FTIR packages. However, it appears that such corrections may not be sufficient. The critical issue is around the central peak of the interferogram, for which the intensity reaching the detector is about twice as large as in the wings of the interferogram. A small error in the measurement of the central peak height results in a small additive (constant or at least smoothly varying) error in the spectrum.⁴⁵⁻⁴⁸ This becomes especially critical i) when taking the ratio of two spectra recorded at a different total intensity (the case in the present work due to the strong change in baseline absorption), and ii) for the parts of the spectrum where the intensity is weak (the case here near 1100 cm^{-1}). Let us suppose that we are comparing two spectra $I_1(\sigma)$ and $I_2(\sigma)$ by plotting the absorption change $\ln[I_1(\sigma)/I_2(\sigma)]$, but the measurement of $I_1(\sigma)$ is spoiled by non-linearity, actually leading to obtaining $I_1(\sigma) + \varepsilon$ instead of $I_1(\sigma)$, where ε is a small quantity, either constant or a slowly varying function of σ . The calculated result is then $\ln\{[I_1(\sigma) + \varepsilon]/I_2(\sigma)\}$, which differs from the correct result by an additive contribution $\ln\{[I_1(\sigma) + \varepsilon]/I_1(\sigma)\} \approx \varepsilon/I_1(\sigma)$, where we have assumed $\varepsilon \ll I_1(\sigma)$.

In the regions where $I_1(\sigma)$ is accidentally small (e.g., near 1100 cm^{-1}), non-linearity of the detector may then lead to spurious peaks (positive or negative, depending on the sign of ε). Once efforts have been made to minimize these non-linear effects at the level of data acquisition, the only possibility left is taking them into account in the fit. Since the data are fitted as the sum of several contributions (pseudo-Voigt functions, generalized trinomial background, component spectra), a convenient method consists of including $1/I_1(\sigma)$ as an additional component spectrum and letting the fit determine the amount ε of the correction as the corresponding extra adjustable parameter.

II - Conditions used for fitting specific spectral regions.—The exact conditions used for fitting the various spectral regions are given here.

vSiO region.—Fitting the vSiO region of the RT data was somewhat difficult, due to the sloping baseline, largely attributable to free-carrier absorption, and to the important absorption from the silicon lattice below 1500 cm^{-1} , which leads to a low IR intensity reaching the detector in this spectral range. Especially, silicon absorption exhibits a peak at 1100 cm^{-1} , which may unduly appear in the absorption spectra because of detector non-linearity (see above) and could be mistakenly interpreted as oxide absorption. We have then fitted the vSiO region as follows: we have taken the spectral interval 880 – 1900 cm^{-1} , excluding the region 1360 – 1700 cm^{-1} , where weak features (plausibly related to electrolyte and O-ring seal absorption) appear. Keeping the region 1700 – 1900 cm^{-1} ensures better reliability of the baseline correction. The TO, LO and D bands were taken as adjustable Gaussian curves, which means 3 adjustable parameters each, while the NBO band was assumed fixed in shape (1 parameter). The baseline was fitted as the linear superposition of 4 components (4 parameters): i) free-carrier absorption, taken as

a Spitzer-Fan shape;^{49,50} ii) 1/reference spectrum), in order to account for detector non-linearity, as explained above; iii) electrolyte absorption, obtained from taking the ratio of the spectra of the empty cell and the filled cell; iv) a “constant” (independent of wave number) contribution. The spectrum obtained just before the negative potential step, for which oxide absorption is maximum, was fitted first, then the other spectra were fitted by starting from the obtained parameters (backwards from spectrum #110 to #41 for the positive potential step, forward from #110 to #400 for the negative step). As done for the SiH fits,⁵ the fits were first carried out by allowing the positions and widths to vary. The results were rather noisy, and especially made correlations between the various Gaussian components appear. In order to reduce this noise, in a second step, the FWHMs of some components were held fixed at their average values (e.g., for the positive-potential step in p polarization, TO component at 95 cm⁻¹ and disorder component at 55 cm⁻¹; hence, the fit involved a total of 12 adjustable parameters for the p-spectra, and 10 for the s-spectra). Also, some of the parameters were occasionally blocked when a fit became unstable; this blocking was made permanent for the next fits by the end of the sequence (typically, spectrum number below 40 or above 350, for which the spectra essentially reduce to noise).

Fitting the 40°C data was still more difficult, because the baseline contribution is larger than at RT, and its shape is largely dominated by the low-energy tail of the Lucovsky-like absorption,⁵ whose exact analytical shape is not known. In practice, the fitting was performed in the interval 880–1360 cm⁻¹, and the baseline was implemented as the sum of three contributions: i) a constant, ii) a broad Gaussian centered at 1500 cm⁻¹ and FWHM 400 cm⁻¹, a simple though admittedly imperfect way to mimic the EL+LL+free-carrier absorption in the range considered. These parameters were chosen from the fits in the regions where no significant amount of oxide is present, iii) an inverted raw spectrum in order to account for problems due to detector non-linearity, in the same way as for the fits of the RT data. The total number of adjustable parameters was then 13 for the p-spectra and 10 for the s-spectra. The results turn out to be critically dependent on the choice of the background. The present choice appears as reasonable, but the relative magnitude of the different vibrational vSiO bands must be regarded as more qualitative than quantitative.

vOH and miscellaneous vibrational bands.—For the RT data, the spectra in the vOH region (2200–4000 cm⁻¹, excluding the interval 2750–2980 cm⁻¹), were fitted as the superposition of a second-order polynomial background, a free-carrier contribution, an electrolyte contribution (known spectrum, taken as an electrolyte spectrum recorded in ATR, multiplied by σ in order to correct for the variable probing depth in the ATR geometry), and two adjustable Gaussian bands. The Gaussian representing the “free” SiOH groups was held fixed at 3600 cm⁻¹, and the other parameters were left free (total number of 10 adjustable parameters). However, near the end of oxide dissolution ($t > 7400$ s), a constraint between the two widths (constant difference) had to be applied to allow for convergence of the fit. The vCH spectra were fitted in the region 2800–3000 cm⁻¹, as the superposition of two Gaussian bands and a second-order polynomial background. The region 1300–1800 cm⁻¹ was fitted by including as component spectra electrolyte absorption for the 8OH₂ band and an inverted reference spectrum (taking into account detector non-linearity), together with a Gaussian band for the strongest band at 1550 cm⁻¹.

III-Assessment of the reliability of the results.—Due to the complexity of our spectra, special attention was paid to the reliability of the fits, and the standard statistical tools (residuals, confidence intervals, correlation matrix) were considered for that purpose.⁴³ Despite the large number of parameters used, it turns out that the results of our fits can be relied upon for the following reasons:

1. Our models are based on well-established results from the literature, and given this information, the number of parameters has been kept to the minimum necessary to obtain satisfactory fits. For example, fitting the vSiO spectra in p polarization would in principle require five bands for NBO, TO, D, and the longitudinal counterparts of TO and D. However, due to the strong overlap of the three higher-energy bands, this number has been reduced to four. Also, for the vOH spectra, the impossibility of obtaining good fits from a combination of two frozen Gaussian bands and electrolyte absorption indicates that more than two types of silanol(ate)s are present. Rather than increasing the number of Gaussian components, we have simply allowed for a variation of the parameters of the two Gaussian components.
2. The uncertainty in the results can be quantitatively assessed from the residuals, the χ^2 2-sigma confidence intervals, and the correlation matrices. Detailed data are given in Supplementary Material I. In brief, the residuals essentially reduce to noise, and the 2-sigma (95%) confidence intervals are at most a few percent for the vSiO spectra at RT, and a few tens of percent for the vSiO spectra at 40°C and the vOH spectra. A few off-diagonal elements of the correlation matrices exceed 0.5. No strong correlations are present for the fits of the vSiO spectra at RT. For the vSiO spectra at 40°C and the vOH data, most important are the correlations among the baseline components, which is of little importance, because the corresponding parameters are mostly a practical way to implement a baseline. However, in some cases, the baseline parameters are correlated with parameters of physical interest: such is the case for the NBO amplitude for the vSiO spectra at 40°C, and the SiOH(hb) parameters for the vOH spectra.
3. As stated in the Experimental section, a very important feature of the present work is the fact that *series of spectra* are fitted. i) An alternative method of assessing the confidence intervals then consists in looking at the “noise” when the parameters are plotted as a function of spectrum number (or as a function of time, see Figs. 4, 6, 7). It can be verified that this simple method leads to results similar to those obtained from the χ^2 test of a single fit. ii) Since the evolution of the spectra is generally weak from one spectrum to the next, the value of each parameter may be averaged over a few consecutive spectra, resulting in statistical reduction of the effective confidence interval (an extreme case being that of parameters that do not appear to change across the cycle, allowing for fixing them at their average value: see, e.g., the TO and LO widths in the fit of the vSiO spectra at RT). iii) Fitting a series of spectra is a stringent test of the stability of the fitting method: if the fit is ill-conditioned, the fitting process unavoidably blows up at some stage of the cycle. Therefore, the fact that our fits are carried out through the cycle with a common method stands as an effective proof of their robustness.
4. Finally, a major concern is about the possible existence of several local minima of the residuals in the parameter space, which would lead to the possibility of converging to alternative parameter sets. In some cases, it has been found indeed that when starting from remote locations in the parameter space, the algorithm may converge indeed to alternative parameter sets. However, such sets turn out to be physically unacceptable (e.g., negative oxide component, or broad band centered way outside the fitting window). In all of the cases, the physically acceptable solution appears to be unique. It is reproducibly obtained when starting from various initial locations in the physically acceptable range of the parameter space, it leads to the lowest minimum of the residuals, and it successfully passes all of the possible physical plausibility tests: the vSiO spectra are characteristic of thin films of anodic silica (strong contributions of NBO and D, slightly lower values of the mean TO-LO frequency and LO-TO splitting as compared to dry bulk amorphous silica, D band shifted downwards in p-polarization as compared to s-polarization); the vSiO integrated p/s intensity ratio is in agreement with the expected high-frequency dielectric constant of 2.2 and the ratios for the Gaussian components are qualitatively consistent with expectation for species located inside the silica layer; the electrolyte contribution from the vOH fits is quantitatively consistent with the data from the 8OH₂ fits and with the amount of dry oxide deduced from the vSiO fits. These various cross-checks stand as a further support of the reliability of our data analysis.

References

1. M. A. Gosálvez, P. Pal, N. Ferrando, H. Hida, and K. Sato, *J. Micromech. Microengin.*, **21**, 125007 (2011).
2. G. T. A. Kovacs, N. I. Maluf, and K. E. Petersen, *Proc. IEEE*, **86**, 1536 (1998).
3. P. Allongue, V. Costa-Kieling, and H. Gerischer, *J. Electrochem. Soc.*, **140**, 1018 (1993).
4. M. Elwenspoek and H. V. Jansen, *Silicon Micromachining, Cambridge Studies in Semiconductor Physics and Microelectronic Engineering*, Cambridge University Press, Cambridge, UK (1998).
5. H. G. G. Philipsen, F. Ozanam, P. Allongue, J. J. Kelly, and J.-N. Chazalviel, *Surf. Sci.*, **644**, 180 (2016).
6. J. Rappich, H. J. Lewerenz, and H. Gerischer, *J. Electrochem. Soc.*, **140**, L187 (1993).
7. W. Haiss, P. Raisch, D. J. Schiffrin, L. Bitsch, and R. J. Nichols, *Faraday Discuss.*, **121**, 167 (2002).
8. H. G. G. Philipsen and J. J. Kelly, *J. Phys. Chem. B*, **109**, 17245 (2005).
9. R. L. Smith, B. Kloock, and S. D. Collins, *J. Electrochem. Soc.*, **135**, 2001 (1988).
10. J.-N. Chazalviel, B. H. Erné, F. Maroun, and F. Ozanam, *J. Electroanal. Chem.*, **509**, 108 (2001).
11. J.-N. Chazalviel, C. da Fonseca, and F. Ozanam, *J. Electrochem. Soc.*, **145**, 964 (1998).
12. D. W. Berreman, *Phys. Rev.*, **130**, 2193 (1963).
13. C. T. Kirk, *Phys. Rev. B*, **38**, 1255 (1988).
14. P. H. Gaskell and D. W. Johnson, *J. Non-Cryst. Solids*, **20**, 171 (1975).
15. K. T. Queeney, M. K. Weldon, J. P. Chang, Y. J. Chabal, A. B. Gurevich, J. Sapjeta, and R. L. Opila, *J. Appl. Phys.*, **87**, 1322 (2000).
16. Y. J. Chabal, *Surf. Sci. Rep.*, **8**, 211 (1988).
17. S. Nihonyanagi, J. A. Mondal, S. Yamaguchi, and T. Tahara, *Ann. Rev. Phys. Chem.*, **64**, 579 (2013).
18. H. Knözinger, in *The Hydrogen Bond*, Vol. III, P. Schuster, G. Zundel, and C. Sandorfy, Editors, p. 1278, North-Holland, Amsterdam, The Netherlands (1976).
19. A. Rimola, D. Costa, M. Sodupe, J.-F. Lambert, and P. Ugliengo, *Chem. Rev.*, **113**, 4216 (2013).
20. R. Outeimabet, M. Cherkaoui, F. Ozanam, N. Gabouze, N. Kesri, and J.-N. Chazalviel, *J. Electroanal. Chem.*, **563**, 3 (2004).
21. J.-N. Chazalviel and F. Ozanam, *J. Electron Spec.*, **54–55**, 1229 (1990).
22. F. Maroun, F. Ozanam, J.-N. Chazalviel, and W. Theiß, *Vibr. Spec.*, **19**, 193 (1999).
23. D. A. G. Bruggeman, *Ann. Phys.*, **24**, 636 (1935).
24. J. E. Bertie and Z. Lan, *Appl. Spec.*, **50**, 1047 (1996) and <http://www.ualberta.ca/~jbertie/IBDownload.HTM> (last accessed April 2015).
25. K. Leung, I. M. B. Nielsen, and L. J. Criscenti, *J. Am. Chem. Soc.*, **131**, 18358 (2009).
26. H. Arm, K. Hochstra, and P. W. Schindlhe, *Chimia*, **28**, 237 (1974).
27. P. D. Lickiss, *Adv. Inorg. Chem.*, **42**, 147 (1995).
28. V. Chandrasekhar, R. Boomishankar, and S. Nagendran, *Chem. Rev.*, **104**, 5847 (2004).

29. D. Aureau, F. Ozanam, P. Allongue, and J.-N. Chazalviel , *Langmuir*, **24**, 9440 (2008).
30. M. Sulpizi, M.-P. Gaigeot, and M. Sprik, *J. Chem. Theory Comput.*, **8**, 1037 (2012).
31. W. M. Young and E. W. Elcock, *Proc. Phys. Soc.*, **89**, 735 (1966).
32. J.-N. Chazalviel, *J. Electrochem. Soc.*, **160**, H159 (2013).
33. R. Outemzabet, M. Cherkaoui, N. Gabouze, F. Ozanam, N. Kesri, and J.-N. Chazalviel, *J. Electrochem. Soc.*, **153**, C108 (2006).
34. A. E. Gershinskii, L. V. Mironova, and E. I. Cherepov, *Phys. Status Solidi (a)*, **38**, 369 (1976).
35. J.-N. Chazalviel, *Surf. Sci.*, **88**, 204 (1979).
36. M. Matsumura and S. R. Morrison, *J. Electroanal. Chem.*, **147**, 157 (1983).
37. T. Dittrich, S. Rauscher, T. Bitzer, M. Aggour, H. Flietner, and H. J. Lewerenz, *J. Electrochem. Soc.*, **142**, 2411 (1995).
38. X. Xia, C. M. A. Ashruf, P. J. French, J. Rappich, and J. J. Kelly, *J. Phys. Chem. B*, **105**, 5722 (2001).
39. X. H. Xia and J. J. Kelly, *Phys. Chem. Chem. Phys.*, **3**, 5304 (2001).
40. R. Memming and G. Schwandt, *Surf. Sci.*, **4**, 109 (1966).
41. E. Peiner and A. Schlauchetzki, *J. Electrochem. Soc.*, **139**, 552 (1992).
42. M. Fertani-Gmati and M. Jemal, *Thermochim. Acta*, **513**, 43 (2011).
43. See, e.g., W. H. Press, S. A. Teukolsky, W. T. Vetterling, and B. P. Flannery, *Numerical Recipes in Fortran. The Art of Scientific Computing*, 2nd ed., chap. 15, Cambridge Univ. Press, Cambridge, UK (1992).
44. F. Ozanam and J.-N. Chazalviel, *Rev. Sci. Instr.*, **59**, 242 (1988).
45. B. Chase, *Appl. Spec.*, **38**, 491 (1984).
46. G. I. Guelachvili, *Appl. Optics*, **25**, 4644 (1986).
47. L. Fiedler, S. Newman, and S. Bakan, *Appl. Optics*, **44**, 5332 (2005).
48. L. Shao and P. R. Griffiths, *Anal. Chem.*, **80**, 5219 (2008).
49. W. Spitzer and H. Y. Fan, *Phys. Rev.*, **108**, 268 (1957).
50. A. Venkateswara Rao, J.-N. Chazalviel, and F. Ozanam, *J. Appl. Phys.*, **60**, 696 (1986).